Highlights

Porosity and free gas estimates from controlled source electromagnetic data at the Scanner Pockmark in the North Sea

Romina A.S. Gehrmann, Giuseppe Provenzano, Christoph Böttner, Héctor Marín-Moreno, Gaye Bayrakci, Yee Y. Tan, Naima K. Yilo, Axel T. Djanni, Karen A. Weitemeyer, Timothy A. Minshull, Jonathan M. Bull, Christian Berndt

- Multidisciplinary approach to estimate physical properties using controlled-source electromagnetic, seismic reflection and core logging data
- In the Scanner Pockmark area in the central North Sea glaciomarine sediment porosity decreases in the top 150 mbsf from 50±10% to 25±3% due to compaction.
- Gas concentration estimated from resistivity models are up to 34±14% in a glacial till deposit, an intermediate reservoir in an active fluid migration and venting system.

Porosity and free gas estimates from controlled source electromagnetic data at the Scanner Pockmark in the North Sea

Romina A.S. Gehrmann[a,1], Giuseppe Provenzano[a,b], Christoph Böttner[c], Héctor Marín-Moreno[d,e], Gaye Bayrakci[d], Yee Y. Tan[a], Naima K. Yilo[a], Axel T. Djanni[a], Karen A. Weitemeyer[a,f], Timothy A. Minshull[a], Jonathan M. Bull[a], Christian Berndt[c]

[a] *University of Southampton, Ocean and Earth Sciences, National Oceanography Centre Southampton, UK*
[b] *Institut des Sciences de la Terre, Université Grenoble Alpes, Grenoble, France*
[c] *GEOMAR, Helmholtz Centre for Ocean Research Kiel, Germany*
[d] *National Oceanography Centre, Southampton, UK*
[e] *Norwegian Geotechnical Institute, Oslo, Norway*
[f] *Ocean Floor Geophysics Ltd, Vancouver, Canada*

Abstract

We present porosity and free gas estimations and their uncertainties at an active methane venting site in the UK sector of the North Sea. In the Scanner Pockmark area in about 150 m water depth, we performed a multidisciplinary experiment to investigate the physical properties of fluid flow structures within unconsolidated glaciomarine sediments. Here we focus on the towed controlled source electromagnetic (CSEM) data analysis with constraints from seismic reflection and core logging data. Inferred background resistivity values vary between 0.6–1 Ωm at the surface and 1.9–2.4 Ωm at 150 mbsf. We calibrate Archie's parameters with measurements on cores, and estimate porosities of about 50±10% at the seafloor decreasing to 25±3% at

[1] R.A.Gehrmann@soton.ac.uk

150 mbsf which matches variations expected for mechanical compaction of clay rich sediments. High reflectivity in seismic reflection data is consistent with the existence of a gas pocket. A synthetic study of varying gas content in this gas pocket shows that at least 33±8% of free gas are required to cause a distinct CSEM data anomaly. Real data inversions with seismic constraints support the presence of up to 34±14% free gas in a 30–40 m thick gas pocket underneath the pockmark within the stratigraphic highs of a till layer above the glacial unconformity in the Aberdeen Ground Formation.
Keywords: North Sea, fluid pathway, electromagnetics, physical properties, resistivity, seismic reflection

1. Introduction

The controlled source electromagnetic (CSEM) method can be used as a powerful constraint on the electrical resistivity of the subsurface, which in the case of marine sediments is largely controlled by sediment porosity and pore fluid composition (*e.g.,* Edwards, 2005). Here, we present porosity and free gas concentration estimates for the first 200 m of unconsolidated sediments at the Scanner Pockmark in the UK licensing block 15/25 in the North Sea (Fig. 1).

Our CSEM experiment forms part of a multidisciplinary study (Robinson et al., in review) to assess the role of vertical/sub-vertical fluid conduits in the integrity of carbon storage sites. Offshore carbon storage sites currently encompass a couple of kilometres deep reservoir rocks sealed with low-permeability cap rocks such as the proposed Golden Eye (Dean & Tucker, 2017) and the active Sleipner (*e.g.,* Boait et al., 2012) sites. To ensure the

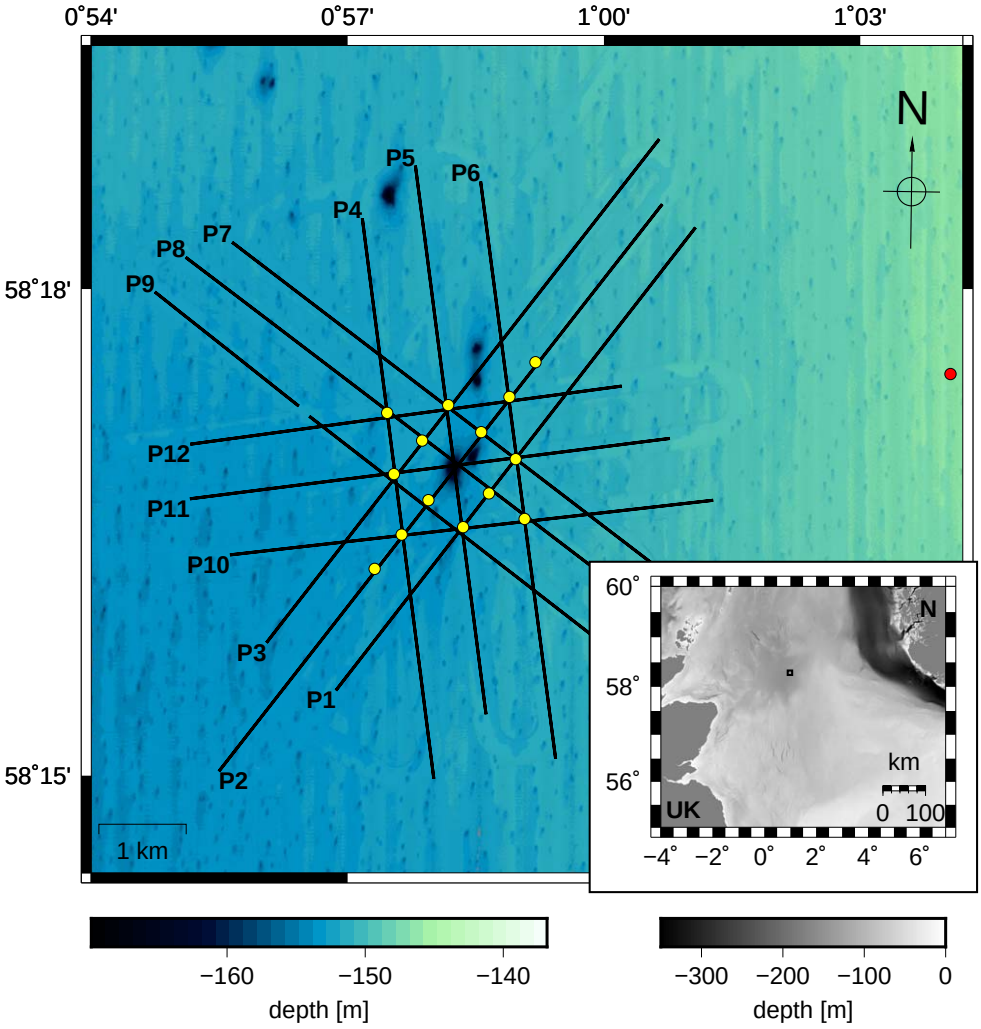

Figure 1: Ship bathymetry at Scanner Pockmark Complex between the UK and Norway in the Central North Sea (position indicated with rectangle in inlay) with collocated CSEM and seismic reflection profiles (black lines) and CSEM ocean bottom instruments (yellow dots) from cruise MSM63 (Berndt et al., 2017). Rock Drill 2 reference drill site from cruise MSM78 (red dot, Karstens et al., 2019).

safety of the CCS sites, assessment of the cap rock on a larger regional scale is required. For example, Karstens & Berndt (2015) have mapped vertical fluid conduits that potentially connect deeper stratigraphic layers with the sediment overburden at about 10 km from Sleipner, and it is therefore important to understand the nature of these conduits.

Focused fluid conduits often show anomalies on seismic images with vertical zones of chaotic reflections, dimmed or wiped-out zones, and bright spots (strong phase reversed reflectors, *e.g.*, White, 1975) at different stratigraphic levels (Cartwright et al., 2007; Løseth et al., 2009; Andresen, 2012). Vertical fluid conduits can be active as short-term blow-out-like events (*e.g.,* resulting in pipe structures offshore Norway, Bünz et al., 2003), or have long-lasting and continuous fluid flow (*e.g.,* the chimney structures above the leaking hydrocarbon reservoir Tommeliten, Arntsen et al., 2007).

Our study area is the Scanner Pockmark site in the Witch Ground Basin and contains a large number of seafloor depressions (pockmarks, Gafeira & Long, 2015; Böttner et al., 2019), of which the larger ones (more than 15 m deep) are related to active ebullition of methane across the seabed (Judd et al., 1994; Li et al., 2020). Sediment deposition in the Witch Ground Basin involves mostly fine-grained material and was rapid during the end of the last glacial period between 15 and 13 ka ago. Within the last 8 ka the area was little affected by erosion nor sedimentation, but methane gas venting from underlying strata was likely active (Hovland & Sommerville, 1985; Judd et al., 1994). In the depths reached by our study (about 150 to 200 mbsf) the following stratigraphic units are identified (Fig. 2) following Stoker et al. (2011) and Böttner et al. (2019): At depth, the Aberdeen Ground Formation

(AGF) is a thick basal quaternary unit with clay-rich layered sediments, whose top represents a regional glacial unconformity. The AGF is interrupted by the Mid Pleistocene Transition ("R4" Reinardy et al., 2017), whose high amplitude reflection suggest the presence of free gas. Tunnel valleys cutting into the AGF are part of the Ling Bank Formation (LBF, Marine Isotope Stage MIS 10-12, 374-478 ka). Above the AGF and LBF, an interval of glacial till deposits (MIS 6, 191 ka) with interrupted layering and variable thickness laterally is thought to act as an intermediate reservoir for shallow gas. The Coal Pit Formation (MIS 3–6, 57–191 ka) is composed of fine-grained glacial tills and contrasts with its transparent to chaotic seismic facies with the MIS 6 deposits. It transitions into the finely laminated seismic reflections of the Swatchway Formation, which were deposited during the last glacial maximum (LGM, MIS 2–3, 29–57 ka). The latest statigraphic unit is the Witch Ground Formation (WGF, MIS 1–2, 29–57 ka) composed of glacial to glaciomarine sediments, characterised with interrupted layering in the lower WGF and composed of horizontally layered glaciomarine to marine sediments of late Pleistocene to Holocene age in the upper WGF. The WGF is mostly eroded at the Scanner Pockmark.

We interpret the physical properties of the unconsolidated, glaciomarine sediments in terms of porosity and gas concentrations and their associated uncertainties. Our approach is to calibrate a rock physics (Archie, 1942) relationship with core logging data to convert resistivity models inferred from CSEM data to porosity. We compare resistivity-derived porosities to trends from mechanical compaction to investigate the dominant factors controlling porosity changes with depth in our study area. To estimate free gas con-

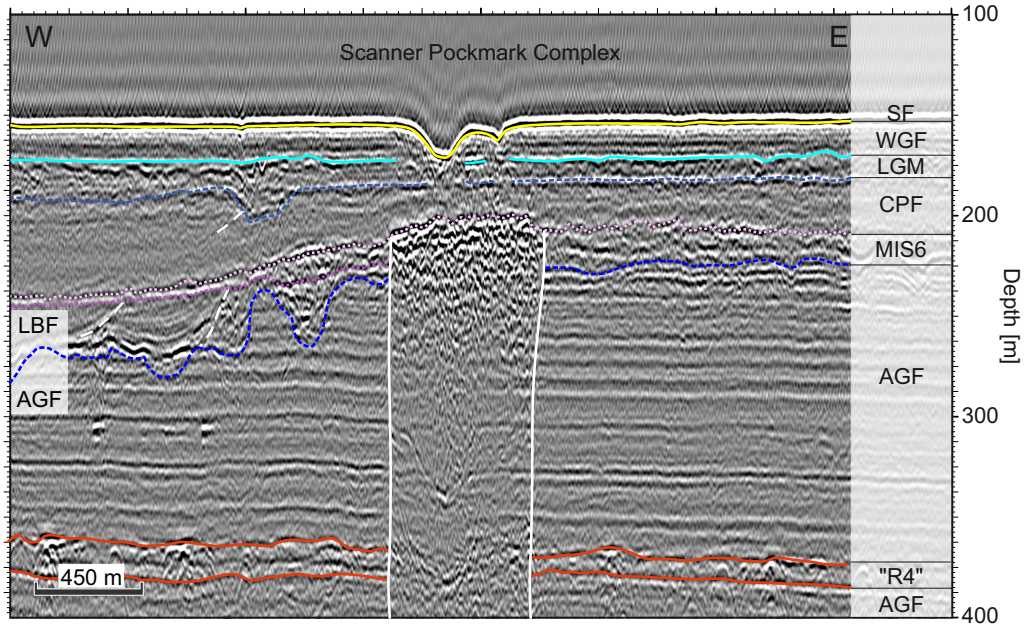

Figure 2: Seismic section across the Scanner Pockmark Complex collocated with CSEM profile P11 (Fig. 1) and main stratigraphic units. Underneath the seafloor (SF, yellow line) starts the Witch Ground Formation (WGF, down to cyan line) and is followed by the Swatchway Formation of the last glacial maximum (LGM, dashed light blue line). Sediments in these top units transition from marine with observed horizontal layering over glaciomarine to glacial deposits with interrupted layering. Below follows the Coal Pit Formation (CPF), a seismically transparent unit, above the top of the MIS 6 till unit (dashed purple line) and the Ling Bank Formation (LBF, filling tunnel valleys). The white lines border the approximate outline of the chimney that is characterised by a bright spot at the top of MIS 6, seismic blanking underneath and discontinuation of the sediment layering in the Aberdeen Ground Formation (AGF, Stoker et al., 2011; Böttner et al., 2019). Layering of the AGF is interrupted with the Mid Pleistocene Transition unit "R4" (red lines, Reinardy et al., 2017).

centrations underneath bright spots observed in the seismic reflection data, we add stratigraphic constraints from the seismic reflection data to the resistivity model. The inferred resistivities are converted to free gas content using Archie's relationship accounting for the uncertainty of each parameter. We also run a synthetic data study to analyse the sensitivity of the CSEM data to free gas abundance. Free gas occurrences are then interpreted in the geological context and contribute to the multidisciplinary analysis (*e.g.,* seismic properties, fluid flow modelling) of the Scanner Pockmark site and to the understanding of the system dynamics (fluid flow cycle, accumulations of free gas in stratigraphic layers, chemistry exchange).

2. Geophysical data analysis

During cruise MSM63 (Berndt et al., 2017) controlled source electromagnetic (CSEM) and active seismic experiments were conducted to analyse the physical properties of the Scanner Pockmark Complex. Combined analysis of the two complementary techniques have shown to improve the interpretation of the pore fluid composition (e.g., Weitemeyer et al., 2011; Goswami et al., 2015; Kannberg & Constable, 2020; Schwalenberg et al., 2020). While seismic reflection data have a much higher resolution to structural changes, CSEM data are especially sensitive to the pore fluid. For example, a few per cent of free gas in the pore space may cause seismic bright spots but only a small response in the CSEM data, while larger amounts of free gas cause no significant additional change in the seismic data, but a strong response in the CSEM data (Constable, 2010). Therefore, CSEM is a powerful tool for hydrocarbon (*e.g.*, MacGregor et al., 2006), fluid flow (e.g., Naif et al., 2015),

groundwater (*e.g.*, Haroon et al., 2018; Gustafson et al., 2019; Micallef et al., 2020) and CCS (*e.g.*, Park et al., 2017; Morten & Bjørke, 2020) studies.

The CSEM experiment at the Scanner Pockmark complex encompassed the Deep-towed Active Source Instrument (DASI, Sinha et al., 1990), two towed electric field receivers (Vulcan, Constable et al., 2016) and 14 ocean bottom instruments from the UK Ocean Bottom Instrument Facility (Fig. 3). The electromagnetic source DASI was powered from the ship through a deep-tow cable. The source emits an up to 110 A square-wave signal with frequencies of 1–256 Hz (of which the fundamental and the first three odd harmonics are chosen for analysis, see section 2.2) from a nearly neutrally-buoyant, 50 m-long antenna. Here, we present the analysis of the data recorded with the two three-axis Vulcan receivers (Constable et al., 2016) towed behind DASI at 197 and 350 m offset (Fig. 3). The CSEM survey was carried out about 20–40 m above the seafloor. The instrument array was towed along twelve profiles in a star pattern across the pockmark at four azimuths (Fig. 1).

2.1. CSEM data processing

The transmitter and receiver data are processed profile by profile for odd harmonic frequencies from the base frequency of 1 Hz up. The raw time series are transformed to the frequency domain applying a Fast Fourier Transform using 1-s long time windows (one period of the square wave signal). The receiver data are then corrected for their frequency-dependent gain function and normalised by the receiver dipole length. The Earth response $C(f)$ is calculated by dividing the receiver response $R(f)$ by the source dipole moment $S(f)$ for each frequency: $C(f) = R(f)/S(f)$ (adapting the routine of Myer et al., 2011). Preliminary analysis of the horizontal electric field E_y

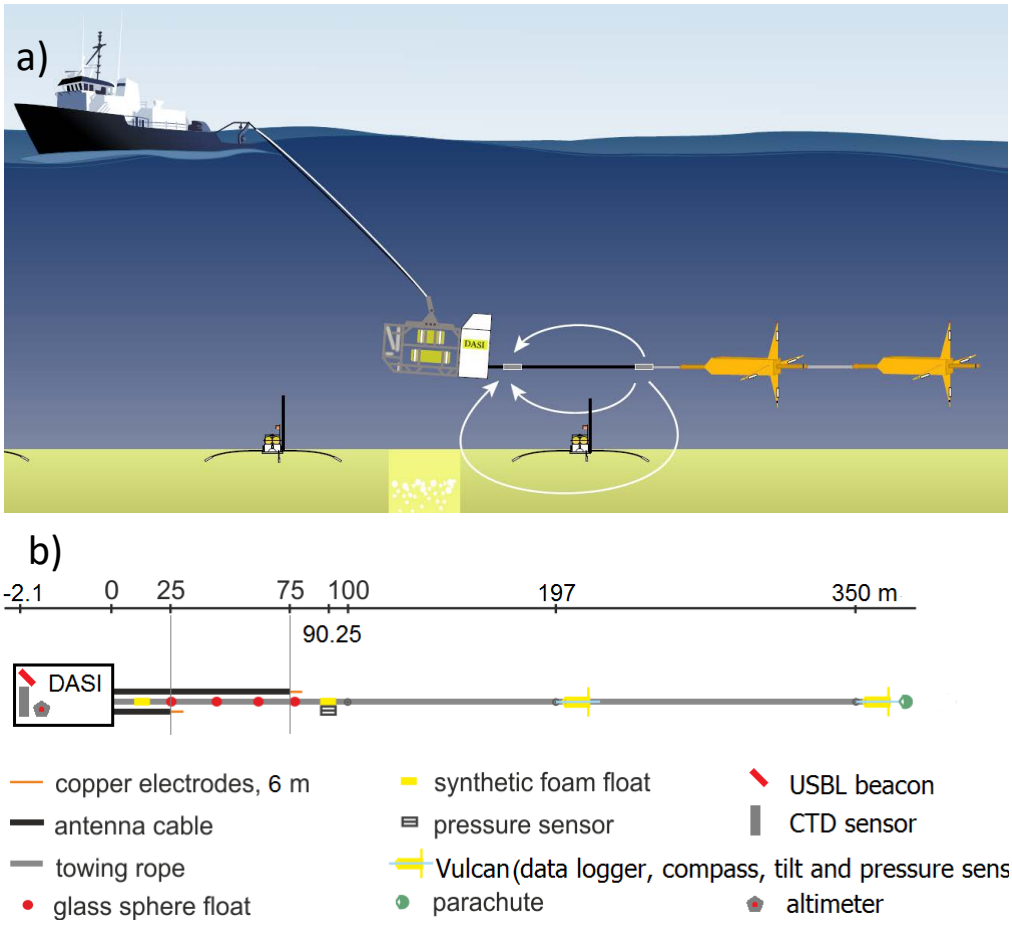

Figure 3: a) Sketch of the survey instrumentation including the electromagnetic source DASI towing the 50-m long antenna (current stream lines are white), and the two Vulcan three-axis electric field receivers, and three-axis electric field electric field ocean bottom receivers across an active venting site (free gas as white bubbles); b) Sketch of DASI-antenna-Vulcan setup with equipment distances. Instrument size not to scale

data (y is defined being inline with the tow direction and the ideal orientation of the source dipole) of both receivers show lower amplitudes than expected, suggesting the possibility of damaged electrodes leading to an equivalent hardware high-pass filtering effect. We, therefore, use the vertical electric field E_z data only. Note, that the 1 m-long vertical antenna of the Vulcan was never in a true vertical position and contains a small part of the E_y signal.

A drift of internal quartz clocks compared to the GPS time was noticed in both receivers after instrument recovery. The data are corrected for this clock drift. Preliminary data analysis suggests that an additional time delay is required to match the phase data. Given this timing uncertainty, we base the interpretations in this paper on amplitudes only but discuss the time delay in Appendix A.

Finally, responses within 30-s long time windows are stacked to improve the signal-to-noise ratio and to estimate a data error from the standard deviation of the stacks. Additionally, navigational uncertainties are estimated using a 2D perturbation study (Gehrmann et al., 2019b), which are added in quadrature to the data errors from the stacking process.

2.2. Air-water boundary effects and choice of frequency range

The time-varying electric current transmitted by a horizontal dipole source causes electromagnetic energy to be coupled inductively perpendicular to the direction of propagation, in the horizontal plane, and galvanically in direction of propagation, in the vertical plane. In water depths less than the receiver offset, a significant amount of the electromagnetic energy measured is guided along the air-water boundary, which due to the large resistivity of the air

layer is dominated by inductive coupling (theory in Chave & Cox, 1982). The energy travelling along the air-water boundary has, therefore, no vertical component so that ideally for a vertical dipole E_z consists solely of energy that has travelled through the seabed and sea water. To the contrary, the measured horizontal component contains a large amount of energy travelled along the air-water boundary due to its amplitude decaying only with $1/r$, where r is the receiver-source offset. In comparison, the energy that travels through the seabed decays exponentially (Weidelt, 2007).

In the measured E_z data, we observe frequencies with high signal-to-noise ratios up to 127 Hz that could potentially be used in the data inversion. Generally, the square wave transmitted has the highest energy in the base frequency (here, 1 Hz) and then falls off as $1/n$, where n is the harmonic number. Higher frequencies often exhibit a smaller signal-to-noise ratio with increasing offset (Myer et al., 2011), and are less sensitive to deeper structure in the seabed (see for example Andréis & MacGregor, 2008). To decide how many frequencies and which range of frequencies to use, we run forward models for a simple model with increasing resistivities with depth and with and without a resistive gas pocket at about 40 mbsf. The differences between these two synthetic data sets are then compared to the data error (Fig. 4 a). This synthetic study demonstrates that frequencies above 7 Hz may not necessarily contain more information (Fig. 4 b and c). For E_z for example, the synthetic data difference is small and varies little for frequencies between 17 and 29 Hz. However, inversion tests suggest that including more frequencies weights information for the higher frequencies more than information for the lower frequencies. Data differences at lower frequencies, however, are

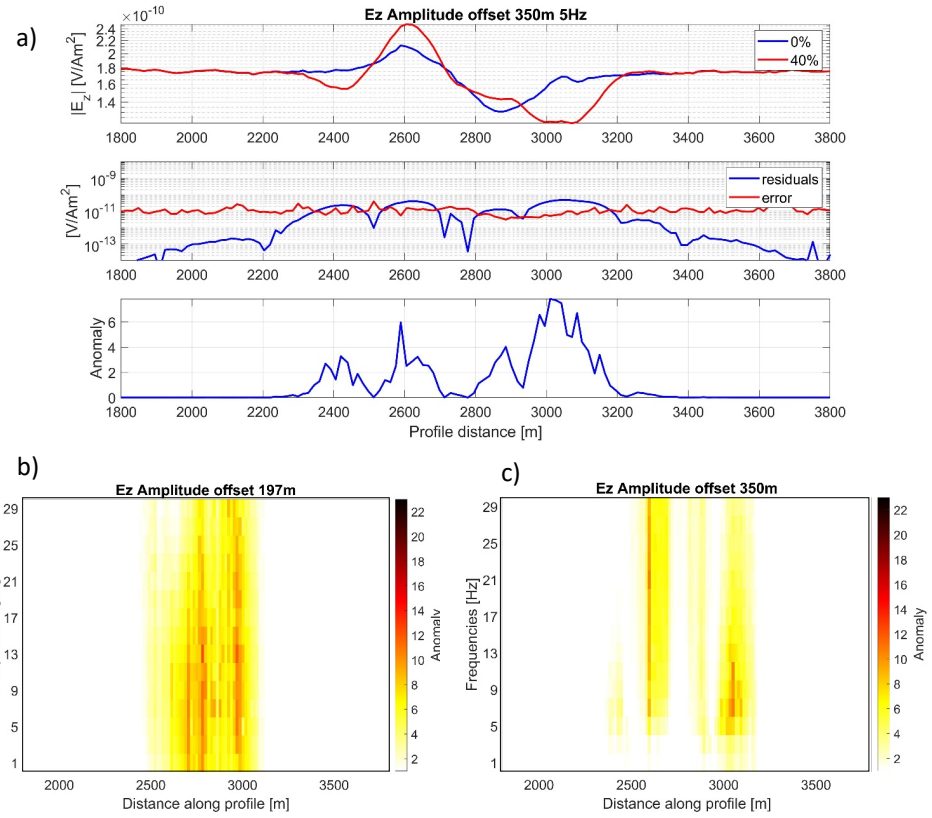

Figure 4: a) Example of synthetic vertical electric field E_z data at 5 Hz (top) for zero and 40% free gas in gas pocket at 40 mbsf; Absolute difference between the data (residuals) compared to realistic data errors (middle), and resulting data anomaly (residuals divided by data errors, bottom); b,c) Data anomaly for synthetic data with and without gas pocket across the pockmark (centred at profile km 2.8) for 1 to 29 Hz for the nearest (b) and the furthest (c) Vulcan.

more diverse, especially at larger offsets. We, therefore, analyse data for frequencies of 1–7 Hz.

2.3. Seismic reflection data analysis

High-resolution reflection 2-D multi-channel seismic (MCS) data have been acquired in lines coincident with the CSEM experiment. An array of two GI-guns of 210 cubic inches each operating in harmonic mode, towed at 2 m depth below the sea surface, was fired with a shot interval ranging between 10.5 and 15 m. The reflected wavefield is acquired by a 150 m-long streamer with 96 channels and a 1.5625 m group spacing. Depth controllers fixed the streamer depth to 2 m below sea surface.

On-board processing of the MCS data included geometry and source-receiver delay corrections, static corrections, common-depth-point (CDP) binning to 1.5625 m, and minimum-phase frequency bandpass filtering with corner frequencies of 25, 45, 420, 500 Hz. Normal move-out correction is applied to CDP gathers, using a simple velocity model of 1488 m/s in the water column (based on sound velocity profiling) and 1500 m/s in the sub-seabed, which is expected to sensibly correct the wavefield kinemactics in the shallow water-saturated subsurface. On-board processing was completed by CDP-stacking and post-stack 2-D Stolt migration (Stolt, 1978). The expected $\lambda/4$ tuning thickness resolution (Kallweit & Wood, 1982) is in the order of 2.5 metres, based on a dominant post-stack frequency of 150 Hz (Berndt et al., 2017).

Post-stack processing included predictive deconvolution to reduce the wavelet duration, and predictive multiple attenuation (Peacock & Treitel, 1969), to eliminate the seafloor reverberation overprinting the subsurface re-

flections with a period of ca. 200 ms. Finally, the data are converted from two-way-traveltime to depth, to use them as a constraint for CSEM resistivity inversion.

2.4. CSEM data inversion

Isotropic resistivity models were obtained using the 2.5-D inversion algorithm MARE2DEM (Key, 2016). The algorithm minimizes the functional U

$$U = \|\mathbf{Rm}\|^2 + \mu \|\mathbf{W}(\mathbf{d} - F(\mathbf{m}))\|^2, \quad (1)$$

where the first term is a measure of the model roughness depending on the resistivity contrasts between model cells $\mathbf{m}$, and the second term measures the data fit, the difference between the observed data $\mathbf{d}$ and the predicted data $F(\mathbf{m})$ weighted by $\mathbf{W}$, a diagonal matrix with the inverse data error. The trade-off between model roughness and the data fit depends on the data error and on the Lagrange multiplier μ, which is estimated intrinsically throughout the inversion. The inversion is based on Occam's razor (Constable et al., 1987), so that the "simplest", in this case, least rough model, is preferred. The optimal model is found in an iterative process linearising the functional U around the current model and then gradually updating it using the Jacobian matrix $\mathbf{J}$, with data sensitivities $J_{ij} = \partial F_i(\mathbf{m})/\partial \mathbf{m_j}$.

The chosen starting models are half spaces with a resistivity of 1 Ωm. The final models seem robust against the choice of starting model as a test with a 10 Ωm-halfspace starting model just results in an increase in the number of iterations. Resistivity models for twelve profiles (Fig. 5) using the towed Vulcan vertical electric field amplitude data for 1 to 7 Hz show an

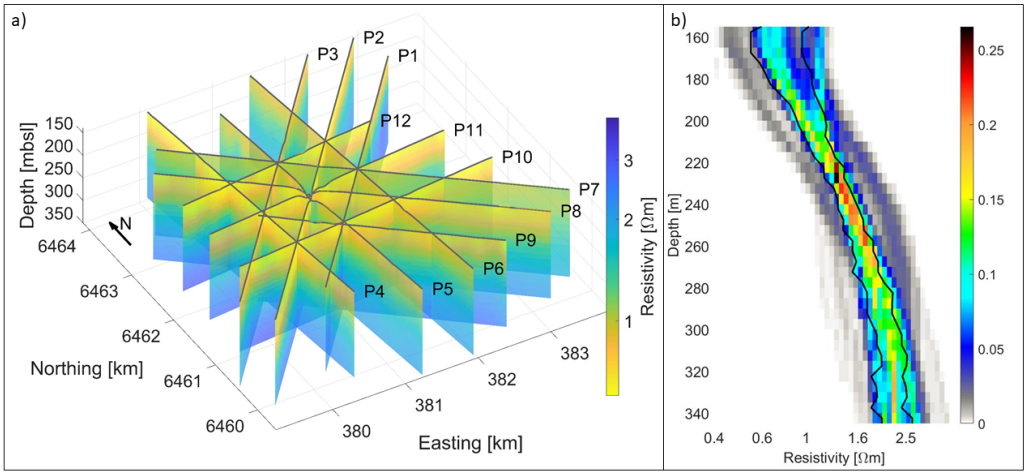

Figure 5: a) Unconstrained resistivity models for all twelve profiles from 2D data inversion; b) Background resistivity probability distribution from resistivity profiles P1–P12 in a) with one standard deviation indicated by black lines.

increase of resistivities with depth from 0.6-1 Ωm at the surface to 2-2.6 Ωm at 200 mbsf. MARE2DEM incorporates anisotropy, but the E_z amplitude data do not require a difference between the vertical and horizontal resistivity, and can be fully explained within the data errors by an isotropic model.

3. Porosity estimation from resistivity and sediment compaction trend

Resistivity can be related to porosity using the empirical Archie's relationship (Archie, 1942; Hearst et al., 2000). The logarithmic expression of Archie's relationship, relating the ratio between the bulk (b) and the fluid (f) resistivity ρ to the porosity ϕ assuming water-saturated sediments,

$$\log_{10}(\rho_\mathrm{b}/\rho_\mathrm{f}) = \log_{10}\mathrm{a} - \mathrm{m}\log_{10}\phi \qquad (2)$$

plots in a straight line (Pearson et al., 1983). Archie's parameters a and m depend on pore connectivity and clay content among other factors. The cementation factor m increases from unconsolidated to cemented sediments.

To calibrate Archie's parameters, we use porosity and resistivity data acquired with the multi-sensor core logger (MSCL) at the British Ocean Sediment Core Research Facility (BOSCORF) on cores from a reference site 6 km to the North East of the pockmark and away from the gas-upwelling area (Fig. 1). The 60-mm-diameter cores were extracted during cruise MSM78 (Karstens et al., 2019) using the remotely operated rock drill 2 system (RD2, British Geological Survey). The RD2 drilled 35 m deep through unconsolidated glaciomarine sediments and tills with at least 24% recovery. The patchy, low-rate recovery is attributed to the presence of intervals dominated by low-cohesion sandy sediments, whose structure did not sustain the drilling stress and which therefore fell out of the core liner during recovery (Karstens et al., 2019).

3.1. Physical parameters from core logging

The sediment cores were logged at intervals of 1 cm using the MSCL (Geotek, 2016) at the BOSCORF laboratory of the National Oceanography Centre Southampton. Bulk density is measured using the gamma ray attenuation method (Evans, 1965) and a 7.6 cm-wide sensor. Porosities are estimated from the measured bulk density D_b using $\phi = (D_\mathrm{b} - D_\mathrm{g})/(D_\mathrm{f} - D_\mathrm{g})$ with grain density $D_\mathrm{g} = 2.65$ g/cm^3 and fluid density $D_\mathrm{f} = 1$ g/cm^3 (Geotek, 2016).

Resistivity is measured by inducing a high-frequency time-varying electric field in the sample. A receiving coil offset by 2 cm detects the magnetic

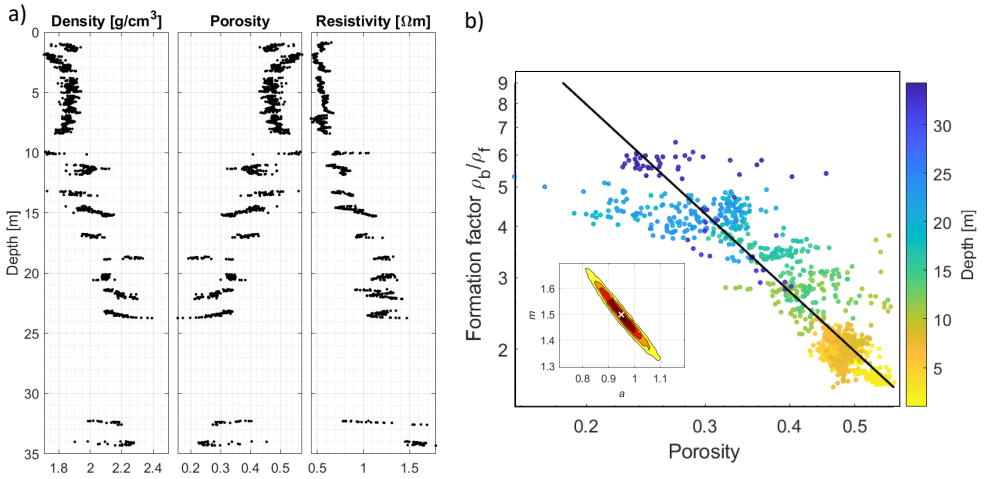

Figure 6: a) Density, density-derived porosity and electrical resistivity from MSCL measurements on sediment cores acquired by drill rig RD2 at a reference site 6 km North East of the pockmark (Karstens et al., 2019); b) Formation factor (bulk vs fluid resistivity ratio) over porosity from MSCL measurements with depth, Archie's empirical relationship (black line) with best-fit Archie parameters a=0.95 and m=1.5 (white cross in probability density of a and m, inlay).

field induced in the sample which is directly proportional to the material conductivity (McNeil, 1980). In order to improve the signal-to-noise ratio, variations attributed to the local environment detected by an identical set of coils operating in air are removed (Jackson et al., 2006).

The MSCL data show an increase in resistivity with depth and a decrease in porosity (Fig. 6 a). For some sections porosities vary over a range of 0.15 and resistivities over 0.4 Ωm, probably due to small sections of unconsolidated material losing integrity and water content after recovery and during core storage.

3.2. Calibration of Archie's parameters

The MSCL data of the unconsolidated sections follow a distinct trend when plotting formation factor (bulk vs fluid resistivity ratio) against porosity (Fig. 6 b) amid the presence of outliers. The fluid resistivity is decreased from 0.278 Ωm measured with DASI's CTD 20 m above the seabed to 0.2 Ωm in the lab due to the temperature increase to 20^{o}C (Riedel et al., 2005; McDougall & Barker, 2011). Archie's relationship (eq. 2) is fit to the data points using a non-linear optimisation technique (adaptive downhill-simplex simulated annealing, Dosso et al., 2001), but other algorithms work as well (such as bootstrapping, Riedel et al., 2020). To explore the ambiguity given the noisiness of the data, we sample interchangeable combinations of a and m and accept the models within the standard deviation of the logging data (similar to Sava & Hardage, 2006; Schwalenberg et al., 2020). The relationship $m = -1.19a + 2.63 \pm 0.04$ is revealed (Fig. 6b inlay) with optimal values of a between about 0.8 and 1.1. These relatively small values of a and m (between 1.3 and 1.7) indicate that the sediment is unconsolidated and the pore space is well interconnected (Pearson et al., 1983).

Archie's relationship can be extended to estimate the gas saturations $S_\mathrm{g} = 1 - S$ in partially saturated sediments with fluid saturation

$$S = \sqrt[n]{a\phi^{-m}\frac{\rho_\mathrm{f}}{\rho_\mathrm{b}}}, \tag{3}$$

where n is the saturation coefficient, which may depend on saturation and reach up to 2.5 (Pearson et al., 1983; Cook & Waite, 2018). Including seismic constraints and resistivities for four layers from the optimal resistivity models, we build synthetic models with a 20–40 m-thick gas pocket at 40 mbsf

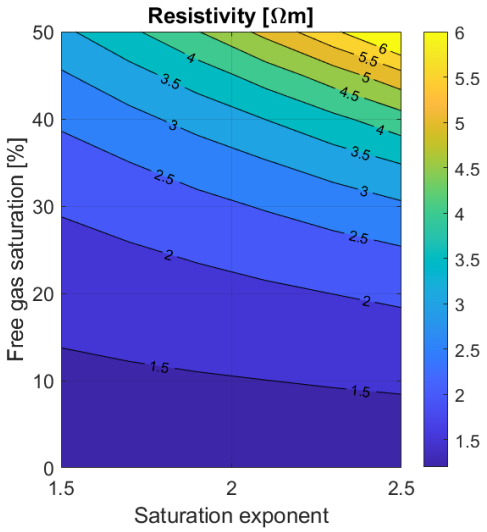

Figure 7: Resistivity from free gas saturation against saturation exponent n from Archie's relationship using 30% porosity, 0.278 Ωm pore water resistivity, a=0.95, and m=1.5.

beneath the pockmark. The background resistivity for the synthetic models at the gas pocket depth is 1.2 Ωm. To relate resistivity to saturation and porosity we use best fit Archie's parameters $a = 0.95$ and $m = 1.5$. The resistivity does not increase much with a few percent of free gas (Fig. 7). For example, 10% of gas only causes an increase from 1.2 to about 1.5 Ωm. For larger saturations the saturation exponent becomes more relevant so that, for this case, saturations between 40% and 50% may cause resistivities from 2.6 to 6.5 Ωm.

3.3. Porosity estimation

The resistivity is sampled from a Gaussian distribution using the 68% confidence interval from the inferred resistivity profiles (Fig. 5 b). Background porosities are estimated using Archie's relationship (eq. 2) and decrease with

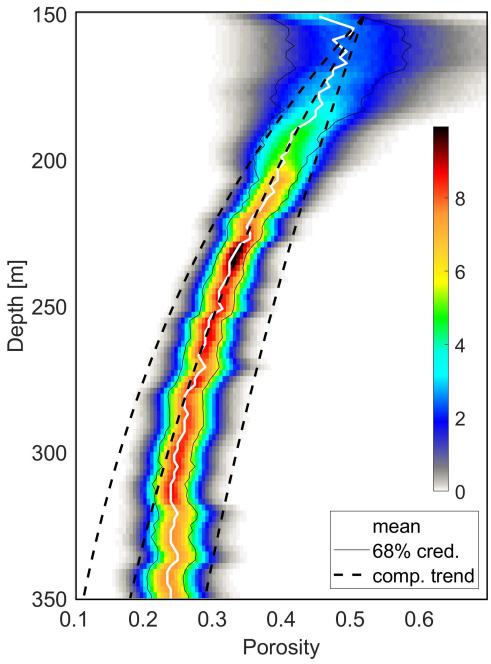

Figure 8: Probability (in per cent for each interval at each depth section) for porosity against depth from background electrical resistivity models (Fig. 5 b) with mean value (white line) and 68% credibility intervals (black lines). Porosity from compaction with depth are shown in dashed lines with compressibility β varying between $2.5 \cdot 10^{-7}$ Pa^{-1} and $6.5 \cdot 10^{-7}$ Pa^{-1}.

depth from about 50±10% at the seafloor to 25±3% at 150 mbsf (Fig. 8).

The resistivity-derived porosities are compared to porosities estimated assuming a sediment compaction vs effective stress relationship $\phi = \phi_0 e^{-\beta\sigma'}$, where the compressibility of saturated sediments is represented by the parameter β, which ranges between $2 \cdot 10^{-6}$ Pa^{-1} for plastic clay to $6.9 \cdot 10^{-8}$ Pa^{-1} for dense clay, and between 10^{-7} Pa^{-1} for loose and $1.3 \cdot 10^{-8}$ Pa^{-1} for dense sand (*e.g.,* Marín-Moreno et al., 2013). Here, we use average values of

2.5–6.5·10^{-7} Pa^{-1} considering the high clay content of the sediment at the Scanner Pockmark (dashed lines Fig. 8). The effective stress σ' is defined as the lithostatic pressure minus the pore water pressure, which under hydrostatic conditions is expressed as $\sigma' = g \cdot (D_b - D_f) \cdot \Delta z$, where Δz is the depth below the seafloor and g is the acceleration due to gravity. Matching porosity results from this relationship and estimates from resistivities suggest that, for the purposes of this study, the sediments between the analysed depths can be represented as a homogeneous medium with porosity changes with depth mainly controlled by mechanical compaction. The deviation from the trend at depths greater 150 mbsf could be related to a loss of CSEM data sensitivity for the short offsets used and a resulting flat resistivity trend.

4. Seismic and electromagnetic data joint interpretation

4.1. CSEM inversion results using seismic constraints

The CSEM inversion algorithm is regularised with the roughness term in eq. 1, promoting a resistivity model with little contrasts. A gas pocket, however, will likely cause a resistivity jump at its top. The inherent ambiguity of CSEM data means that models with either a gradual or a sharp resistivity increase can explain the observed data. Increasing the roughness at that boundary will therefore result in a more geologically reliable result. The geological boundary can be extracted from seismic reflection data because seismic impedance also changes at the gas pocket and causes a bright phase-reversed reflector (*e.g.,* Gehrmann et al., 2019a). Inversions allowing a roughness increase at the bright spot at about 40 mbsf result in a resistivity jump (shown for P5 and P11 in Fig. 9 and for four profiles across the

pockmark on Fig. 10).

4.2. Free gas estimation

Inversions of the synthetic data (Fig. 11) with realistic errors for gas pockets (here, top and bottom constraint) with variable resistivity show that data anomalies caused by small resistivity contrasts such as between 1.2 and 1.9 Ωm (18–28% free gas, using eq. 3 and a=0.95, m=1.5, and n=2) are below the data error and cannot be resolved. They also show that an increase to 2.5 Ωm or 25–40% free gas are sufficient to be resolved. We conclude that at least 33±8% gas saturation is required to be resolved. Including a constraint for the bottom of the gas occurrence in the real data inversion leads to an increase in resistivity for P5 and P2 (Fig.10 right), but not for P8 and P11. Reasons for this could be that the amount of gas is at the limit of the data sensitivity and that it is less clear from seismic data that there is a sharp lower boundary. The following interpretation is therefore done from inversion results with top constraints only.

Resistivity models inferred for profiles P2, P5, P8 and P11 using the bright spot as a constraint (Fig. 10) result in free gas estimations of up to 34% (Fig. 12). Absolute uncertainty estimates (e.g., Malinverno et al., 2008) are based on adding the uncertainty for each parameter in eq. 3 (by taking the respective derivative and multiplying it with the standard deviation estimate) and reach up to 14 %. The main contributors to the uncertainty are the standard deviation of the inferred resistivity (Fig. 5 b) and porosity (Fig. 8). The thickness of the free gas saturated layer varies between 30 to 40 m underneath the pockmark when considering only gas estimations above their uncertainty. Along profile P8 towards the NWW the thickness may reach up

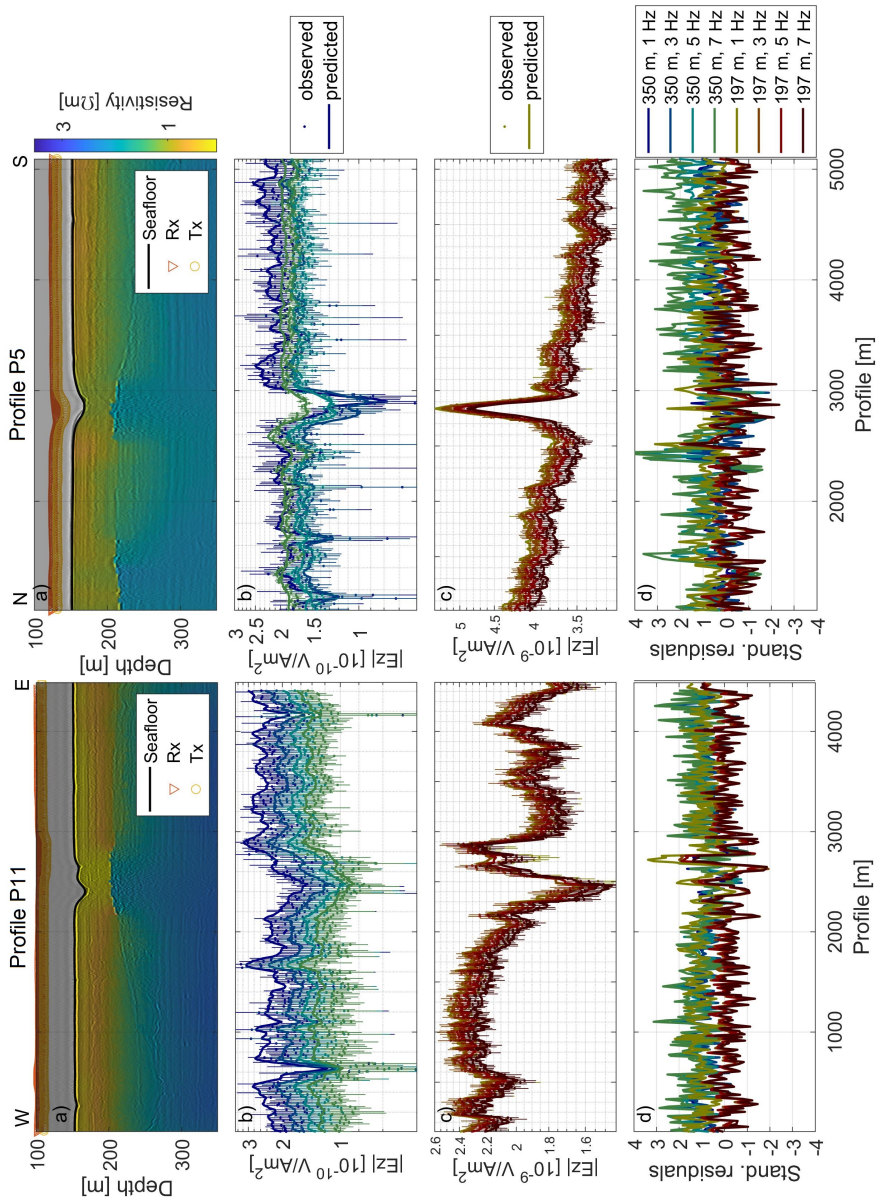

Figure 9: Resistivity models (a) and vertical electric field amplitudes (b–d) for CSEM perpendicular profiles P11 (left) and P5 (right) with seismic constraints. The amplitudes for the vertical electric field E_z are shown on panel b for the furthest Vulcan and c for the closest Vulcan, for observed (dots with error bars) and predicted data (solid lines). Standardised residuals for both receivers are shown on panel d. E_z is sensitive to the tilt of the instrument, which explains the amplitude peaks and troughs when the instrument adjusts above small and large pockmarks.

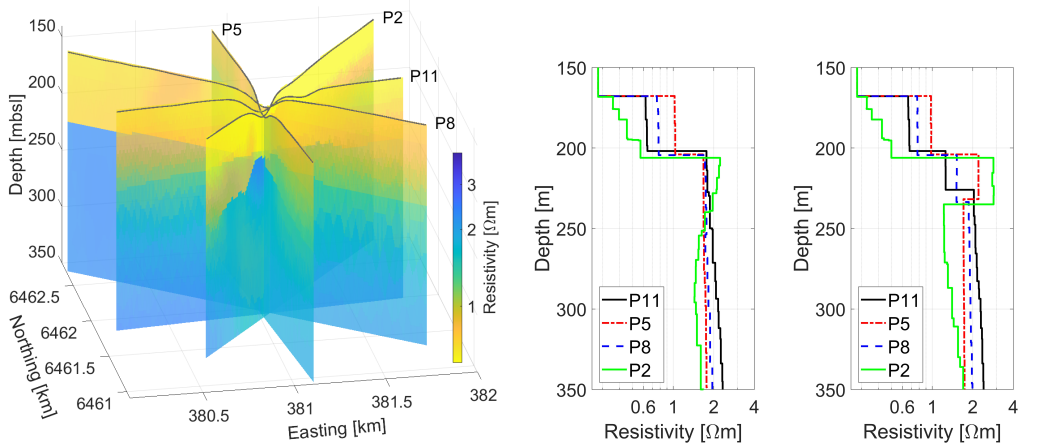

Figure 10: Left: Seismically constrained resistivity models for four profiles across the Scanner Pockmark; Middle: Vertical resistivity profiles from the centre of the pockmark; Right: Vertical resistivity profiles from the centre of the pockmark from inversion including a bottom constraint for the gas pocket.

to 70 m.

5. Discussion

We present an estimation of porosity from towed CSEM data down to 200 mbsf. CSEM data for all profiles can be explained with a gradual resistivity increase with depth (Fig. 5). Resistivities increase from 0.6-1 Ωm, typical for unconsolidated marine sediments, at the surface to 2-2.6 Ωm at 200 mbsf. The resistivity increase flattens out below 150 mbsf, which could also be explained by reaching the penetration limit controlled by the maximum dipole-dipole offset of only about 300 m. When the data sensitivity is reduced the roughness term in eq. 1 is weighted stronger and penalizes resistivity change.

Porosity estimation from resistivity profiles requires calibration of Archie's

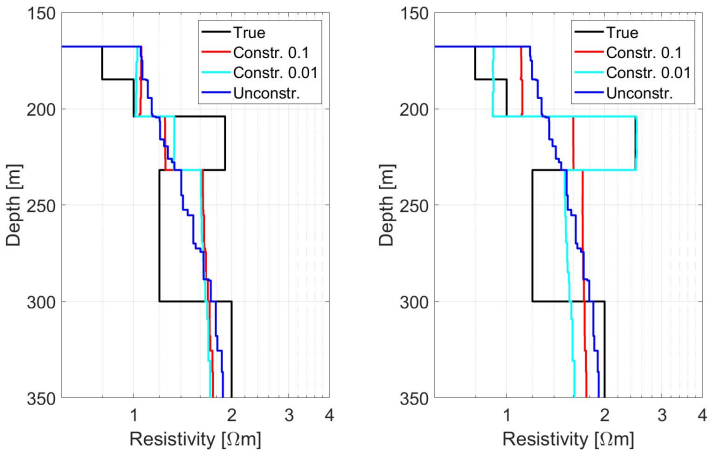

Figure 11: Vertical resistivity depth profiles at the centre of the pockmark for synthetic data inversion for the true model (black line) with realistic data error, for an unconstrained model (blue line) and including seismic constraints. The roughness is reduced above and below the gas pocket at about 210 mbsl and about 235 mbsl with the MARE2DEM-specific multiplier 0.1 (red line) and 0.01 (turquoise line). Left: Result for small increase in resistivity in gas pocket; Right: Result for larger increase in resistivity and higher free gas concentration.

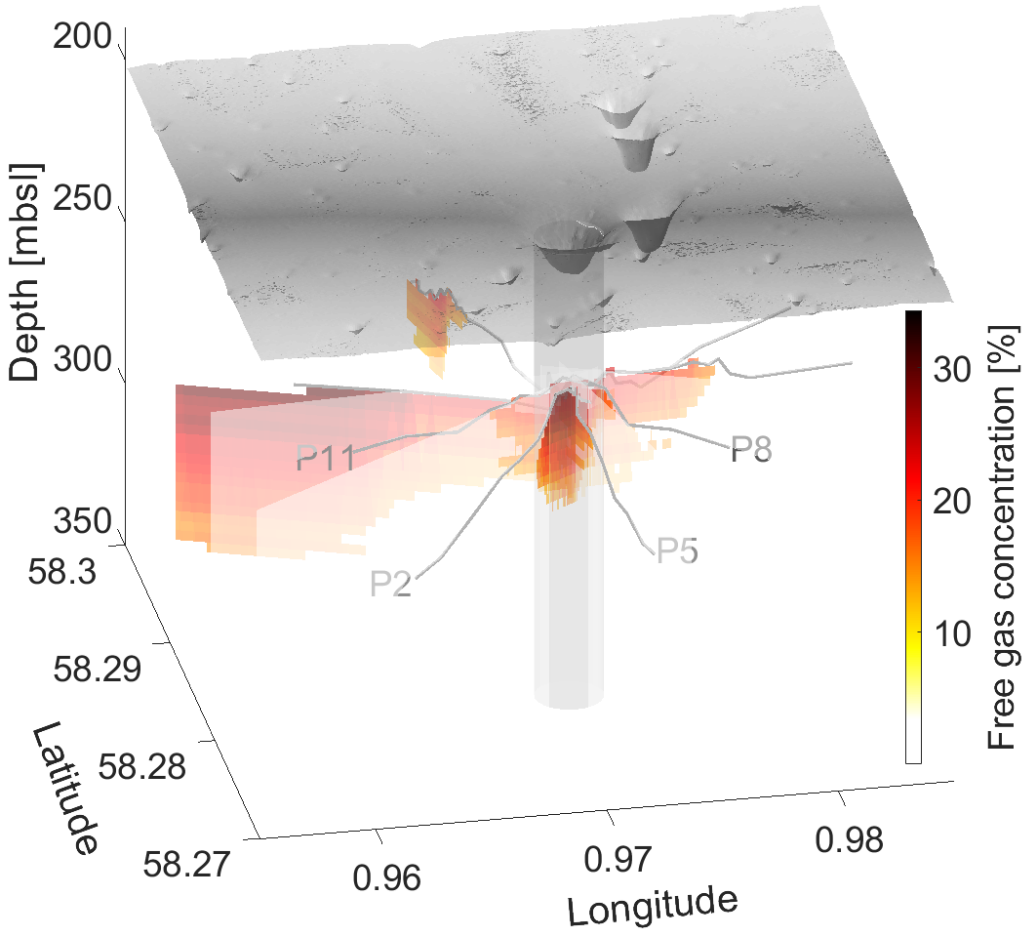

Figure 12: Free gas estimation above their uncertainty for profiles P2, P5, P8 and P11 across the Scanner Pockmark using resistivity model and optimal Archie parameters a=0.95, m=1.5, and n=2. Bathymetry and approximate location of vertical fluid conduit in grey. Grey lines refer to the top of the gas bearing layer in glacial tills underneath the Coal Pit Formation and above the Aberdeen Ground Formation.

parameters using logging data (*e.g.,* Riedel et al., 2005). We use MSCL data from cores extracted at a reference site about 6 km from the Scanner Pockmark. The cores do not show degassing structures, but are incomplete having lost sandy sections and loosing integrity at the borders of intact sediment sections, which likely causes the few outliers in the data (Fig. 6). The resistivity-porosity trend (Fig.6 b), however, is evident and can be fit with Archie's relationship using best fit Archie's parameters a=0.95 and m=1.5, reasonable values for unconsolidated sediments with well-connected pore space (Hearst et al., 2000). Porosity decreases with depth from 50±10% at the seafloor to 25±3% at 150 mbsf and match values from a porosity vs effective stress relationship well suggesting that low frequency porosity changes throughout the sediments in the first 150 m are mainly controlled by mechanical compaction. The best fit is reached for a value for β =4.5·10^{-7} Pa^{-1} indicating that the compressibility of the sediment is larger than for loose sand due to the high content of fine-grained components (*e.g.* Marín-Moreno et al., 2013).

Porosities from this mechanical compaction relationship start deviating from the resistivity derived porosities below ∼150 mbsf likely due to the reduction of CSEM data sensitivity. Resistivities would require to increase further with depth to follow the compaction trend. Increasing data sensitivity below 150 mbsf requires including larger offset data from the ocean bottom instruments.

Inferred resistivity models are ambiguous and depend on the inversion algorithm choice (*e.g.,* Constable et al., 2015). Ambiguity can be addressed using prior constraints, for example, resistivity limits from logging data (*e.g.*, Schwalenberg et al., 2020), or structural constraints from seismic reflection

data (*e.g.,* Gehrmann et al., 2019a). We use collocated seismic reflection data from the same cruise MSM63 (Berndt et al., 2017) with a vertical resolution of about 2.5 m. Seismic reflection data in this case can constrain the resistivity model by adding information about the boundary to the gas bearing layer, which is a contrast in resistivity and in seismic velocity alike. Strongly reducing the smoothness regularisation at the layer causes the inversion to find an optimal model close to the true model (Fig. 11).

To study the sensitivity of the CSEM data to a shallow gas pocket, two synthetic studies were performed. First, forward modelling for a model with and without a shallow gas pocket was used to estimate the optimal frequency range of the vertical electric field amplitude data. The result (Fig. 4) suggests that frequencies from 1 to 7 Hz have the most diverse information content about the gas pocket, while higher frequencies, although strongly present in the data, seem to have redundant information. Second, synthetic data inversion for a model containing a shallow gas pocket with varying gas content (Fig. 11) suggest that $\sim$33$\pm$8% of gas are required to cause a data anomaly larger than the data error. For CSEM the product of resistivity and layer thickness can be better resolved than each parameter individually (Edwards, 1997), so that different combinations of resistivity and thickness may be equivalent. A model with a gas pocket will be interpreted as a gradual change when not using seismic constraints (Fig. 11) because the inversion algorithm minimises the roughness term as well as the data fit (eq.1).

The data errors for the towed, vertical electric field amplitude data were estimated with a 2D perturbation study (Gehrmann et al., 2019b) to encompass navigation uncertainties, and are relatively large for the furthest Vulcan

(about 10%) and only a few percent for the closest Vulcan (Fig. 9), which causes the data from the closest Vulcan to be generally better fit than data from the furthest one with slightly biased standardised residuals (Fig. 9d). For real data inversions, the data fit for all profiles is comparable, for example, perpendicular profiles P11 and P5 shown in Fig. 9, where the source was towed at different heights above the ground (40 and 20 m respectively). The ambiguity for different constraints is evident. For example, including constraints from seismic data at the high amplitude reflection beneath the pockmark on profile P11 (Fig. 9 left) shows that resistivities are lower for the sediment column above the reflector than next to the pockmark where resistivities increase gradually. Including a bottom constraint for the gas pocket leads to the inferred model to have a step-wise increase of resistivity with depth (Fig. 10 right), while the inversions for P2 and P5 converge to a model including a resistive layer. The observed ambiguity is increased by using only E_z amplitude data (uncertainty in phase data discussed in Appendix A), and could be addressed by including ocean bottom instrument data in the future, and also because the bottom of the gas bearing layer is not well constraint. Optimal models for all profiles agree well when including only the constraint for the top of the resistive layer (Fig. 10 left).

Gas estimations (Fig. 12) from CSEM data suggest a 30–40 m thick gas pocket (for gas estimates larger than their uncertainty). The maximum thickness of the gas layer is estimated to be $\sim$70 m along profile P8 towards the NWW. When the gas column reaches a thickness and a pressure high enough to overcome the capillary entry pressure the gas moves vertically through the clay dominated glacial tills of the Coal Pit and Swatchway Formation and

form pockmarks at the surface (Fig. 13). We expect the gas bearing layer to be within a few 10s of metres thick based on thickness directly related to the pressure required to fracture the cap rock or to overcome the capillary entry pressure (e.g., Zhang & Sanderson, 2002). Li et al. (2020) have observed continuous venting extrapolated to 1.6–2.7 10^6 kg/year. To support the continuous venting requires that the shallow reservoir is constantly fed from deeper sources. While evidence of active fracturing has not been observed on high-frequency methods such as parasound data (Böttner et al., 2019), shear wave splitting and P-wave velocity anisotropy in the upper 40 mbsf below the pockmark (Bayrakci et al., 2020) suggest the presence of fractures.

Although gas estimations from the inferred resistivity models using seismic constraints (Fig.12) come with an absolute uncertainty of up to 14%, the fact that they are up to 34% is a robust indicator for gas accumulating in the stratigraphic highs in the glacial tills just above the Aberdeen Ground Formation (Fig. 13). Combined seismic and CSEM data interpretation suggest that the gas pocket has an irregular shape reaching 500 m to 700 m in width on profiles P5, P2 and P11, but extending to the NWW on profile P8 along a stratigraphic high. Several profiles suggest the presence of free gas in the glacial tills without a pockmark directly above indicating lateral movement of the gas within the tills.

6. Conclusions

The Scanner Pockmark area is abundant in small and large pockmarks, the latter connected to deep reaching vertical/subvertical fluid conduits that act as pathways for methane gas venting at the surface. At an impermeable

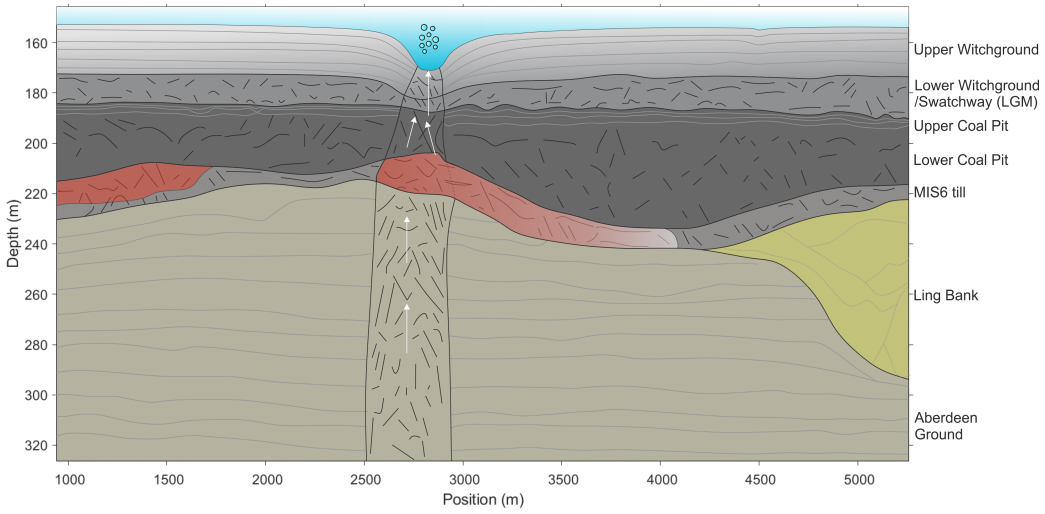

Figure 13: Sketch of gas accumulations (red) in the glacial till layer (M1S6) between the clay-dominated Aberdeen Ground and Coal Pit Formations. The gas migrates (white arrows) vertically from deeper sources through the fluid pathway (seismic chimney, black vertical lines), causing active venting at the pockmark.

sediment interval, the glaciomarine Coal Pit Formation, free gas accumulates forming a gas pocket before breaching occurs and the gas reaches the surface. Here, we show how towed controlled-source electromagnetic data can be used to estimate the background porosity and the free gas content. Both are estimated using Archie's relationship by calibrating Archie's parameters with core logging data. Inversion of vertical electric field amplitude data of twelve profiles gives a background resistivity trend increasing from 0.6–1 Ωm at the surface to 1.9–2.4 Ωm at 150 mbsf. Considering the uncertainties of resistivity and Archie's parameters, porosity is estimated to decrease from about 50±10% at the seafloor to 25±3% at 150 mbsf, which matches porosity estimates from mechanical compaction of clay rich sediments.

Resistivity models constrained with structural information from seismic reflection data suggest a resistive area at about 40 mbsf at the pockmark that can be interpreted as a shallow gas pocket. A synthetic data study shows that at least 33±8% free gas is required to cause an anomaly in the CSEM data large enough to be inferred in the inversion. Gas concentrations are estimated to be at the resolution limit for all four profiles across the pockmark supporting gas accumulations 30–40 m thick with up to 34±14% free gas (Fig 12 and Fig. 13) that act as an intermediate reservoir for the gas to migrate from greater depth to the surface and cause observed venting at the surface.

Acknowledgments

We would like to thank the MSM63 and MSM78 cruise crews and scientific parties, especially the Ocean Bottom Instrument Consortium team and

Laurence North for CSEM instrumentation support, the GEOMAR seismic data acquisition and processing team, and the BGS Rock Drill 2 team. We thank the British Ocean Sediment Core Research Facility team, especially Millie Watts, for the core data and the helpful discussions. We are grateful to Steven Constable from Scripps Institution of Oceanography, USA, for advice and lending eight CSEM data loggers for the survey. CSEM processing and inversion input routines are based on scripts by David Myer and Kerry Key. This work was supported by the European Commission through Horizon 2020 project STEMM-CCS (grant agreement No. 654462) and NERC grant NE/N01610/1. We acknowledge the use of the IRIDIS High Performance Computing Facility, and associated support services at the University of Southampton, in the completion of this work.

References

Andréis, D., & MacGregor, L. (2008). Controlled-source electromagnetic sounding in shallow water: Principles and applications. *Geophysics*, *73*, F21–F32.

Andresen, K. J. (2012). Fluid flow features in hydrocarbon plumbing systems: What do they tell us about the basin evolution? *Marine Geology*, *332*, 89–108.

Archie, G. E. (1942). The Electrical Resistivity Log as an Aid in Determining Some Reservoir Characteristics. *Trans. Am. Inst. Min. Metall. Pet. Eng.*, *146*, 54–62.

Arntsen, B., Wensaas, L., Løseth, H., & Hermanrud, C. (2007). Seismic

modeling of gas chimneys. *GEOPHYSICS*, *72*, SM251–SM259. doi:10.1190/1.2749570.

Bayrakci, G., Minshull, T. A., Bull, J. M., Henstock, T. J., Provenzano, G., Birinci, H., Macdonald, C., & Dunn, R. (2020). P-wave velocity anisotropy in an active methane venting pockmark: The Scanner Pockmark, northern North Sea. EGU2020online. doi:10.5194.

Berndt, C., Elger, J., Böttner, C., Gehrmann, R., Karstens, J., Muff, S., Pitcairn, B., Schramm, B., Lichtschlag, A., & Völsch, A. (2017). RV MARIA S. MERIAN Fahrtbericht / Cruise Report MSM63 - PERMO, Southampton – Southampton (U.K.) 29.04.-25.05.2017. GEOMAR Report N.Ser. 037. doi:10.3289.

Bünz, S., Mienert, J., & Berndt, C. (2003). Geological controls on the Storegga gas-hydrate system of the mid-Norwegian continental margin. *Earth and Planetary Science Letters*, *209*, 291 – 307. doi:https://doi.org/10.1016/S0012-821X(03)00097-9.

Boait, F. C., White, N. J., Bickle, M. J., Chadwick, R. A., Neufeld, J. A., & Huppert, H. E. (2012). Spatial and temporal evolution of injected CO2 at the Sleipner Field, North Sea. *Journal of geophysical research: solid earth*, *117*.

Böttner, C., Berndt, C., Reinardy, B. T., Geersen, J., Karstens, J., Bull, J. M., Callow, B. J., Lichtschlag, A., Schmidt, M., Elger, J., Schramm, B., & Haeckel, M. (2019). Pockmarks in the Witch Ground Basin, Central

North Sea. *Geochemistry, Geophysics, Geosystems*, *20*, 1698–1719. doi:10.1029/2018GC008068.

Cartwright, J., Huuse, M., & Aplin, A. (2007). Seal bypass systems. *AAPG Bulletin*, *91*, 1141–1166. doi:10.1306/04090705181.

Chave, A. D., & Cox, C. S. (1982). Controlled Electromagnetic Sources for Measuring Electrical Conductivity Beneath the Oceans 1. Forward Problem and Model Study. *Journal of Geophysical Research*, *87*, 5327–5338.

Constable, S., Orange, A., & Key, K. (2015). And the geophysicist replied:"Which model do you want?". *Geophysics*, *80*, E197–E212.

Constable, S. C. (2010). Ten years of marine CSEM for hydrocarbon exploration. *Geophysics*, *75*, 75A67–75A81.

Constable, S. C., Kannberg, P. K., & Weitemeyer, K. (2016). Vulcan: A deep-towed CSEM receiver. *Geochemistry, Geophysics, Geosystems*, *17*, 1042–1064. doi:10.1002/2015GC006174.

Constable, S. C., Parker, R. L., & Constable, C. G. (1987). Occam's inversion: A practical algorithm for generating smooth models from electromagnetic sounding data. *Geophysics*, *52*, 289–300.

Cook, A. E., & Waite, W. F. (2018). Archie's Saturation Exponent for Natural Gas Hydrate in Coarse-Grained Reservoirs. *Journal of Geophysical Research: Solid Earth*, *123*, 2069–2089. doi:10.1002/2017JB015138.

Dean, M., & Tucker, O. (2017). A risk-based framework for Measurement, Monitoring and Verification (MMV) of the Goldeneye storage complex for

the Peterhead CCS project, UK. *International Journal of Greenhouse Gas Control*, *61*, 1 – 15. doi:https://doi.org/10.1016/j.ijggc.2017.03.014.

Dosso, S. E., Wilmut, M. J., & Lapinski, A.-L. S. (2001). An Adaptive-Hybrid Algorithm for Geoacoustic Inversion. *Oceanic Engineering, IEEE Journal of*, *26*, 324–336.

Edwards, R. N. (1997). On the resource evaluation of marine gas hydrate deposits using sea-floor transient electric dipole-dipole methods. *Geophysics*, *62*, 63–74.

Edwards, R. N. (2005). Marine Controlled Source Electromagnetics: Principles, methodologies, future commercial applications. In *Surveys in Geophysics* (pp. 675–700). Berlin, Heidelberg, New York: Springer volume 26.

Evans, H. (1965). Grape - a device for continuous determination of material density and porosity. In *Proceedings of 6th Annual SPWLA Logging Symposium. Dallas, TX.* (pp. B1–B25). volume 2.

Gafeira, J., & Long, D. (2015). Geological investigation of pockmarks in the Scanner Pockmark SCI area. *JNCC Report*, *570*.

Gehrmann, R. A., Schnabel, C., Engels, M., Schnabel, M., & Schwalenberg, K. (2019a). Combined interpretation of marine controlled source electromagnetic and reflection seismic data in the German North Sea: a case study. *Geophysical Journal International*, *216*, 218–230.

Gehrmann, R. A. S., Haroon, A., Morton, M., Djanni, A. T., & Minshull, T. A. (2019b). Seafloor massive sulphide exploration using deep-towed

controlled source electromagnetics: navigational uncertainties. *Geophysical Journal International*, *220*, 1215–1227. doi:10.1093/gji/ggz513.

Geotek (2016). Multi-Sensor Core Logger - Manual.

Goswami, B. K., Weitemeyer, K. A., Minshull, T. A., Sinha, M. C., Westbrook, G. K., Chabert, A., Henstock, T. J., & Ker, S. (2015). A joint electromagnetic and seismic study of an active pockmark within the hydrate stability field at the Vestnesa Ridge, West Svalbard margin. *Journal of Geophysical Research: Solid Earth*, *120*, 6797–6822.

Gustafson, C., Key, K., & Evans, R. L. (2019). Aquifer systems extending far offshore on the US Atlantic margin. *Scientific reports*, *9*, 1–10.

Haroon, A., Lippert, K., Mogilatov, V., & Tezkan, B. (2018). First application of the marine differential electric dipole for groundwater investigations: A case study from Bat Yam, Israel. *Geophysics*, *83*, B59–B76. doi:10.1190/geo2017-0162.1.

Hearst, J. R., Nelson, P. H., & Paillet, F. L. (2000). *Well Logging for Physical Properties*. (2nd ed.). Hoboken, N.J.: John Wiley.

Hovland, M., & Sommerville, J. H. (1985). Characteristics of two natural gas seepages in the North Sea. *Marine and Petroleum Geology*, *2*, 319 – 326. doi:10.1016/0264-8172(85)90027-3.

Jackson, P. D., Lovell, M. A., Roberts, J. A., Schultheiss, P. J., Gunn, D., Flint, R. C., Wood, A., Holmes, R., & Frederichs, T. (2006). Rapid non-contacting resistivity logging of core. In *New Techniques in Sediment Core*

Analysis (pp. 209–217). Geological Society London, Special Publication volume 267.

Judd, A. G., Long, D., & Sankey, M. (1994). Pockmark formation and activity, UK block 15/25, North Sea. *Bulletin of the Geological Society of Denmark*, *41*, 34–49.

Kallweit, R., & Wood, L. (1982). The limits of resolution of zero-phase wavelets. *Geophysics*, *47*, 1035–1046.

Kannberg, P. K., & Constable, S. (2020). Characterization and quantification of gas hydrates in the california borderlands. *Geophysical Research Letters*, *47*, e2019GL084703. doi:10.1029/2019GL084703.

Karstens, J., & Berndt, C. (2015). Seismic chimneys in the Southern Viking Graben – Implications for palaeo fluid migration and overpressure evolution. *Earth Planet. Sci. Lett.*, *412*, 88–100.

Karstens, J., Böttner, C., Edwards, M., Falcon-Suarez, I., Flohr, A., James, R., Lichtschlag, A., Maicher, D., Pheasant, I., Roche, B., Schramm, B., & Wilson, M. (2019). RV MARIA S. MERIAN Fahrtbericht / Cruise Report MSM78 - PERMO 2, Edinburgh – Edinburgh (U.K.) 16.10.-25.10.2018. GEOMAR Report N.Ser. 048. doi:10.3289/GEOMAR_REP_NS_48_2019.

Key, K. (2016). MARE2DEM: A 2-D inversion code for controlled-source electromagnetic and magnetotelluric data. *Geophysical Journal International*, *207*, 571–588. doi:10.1093/gji/ggw290.

Li, J., Roche, B., Bull, J. M., White, P. R., Leighton, T. G., Provenzano, G., Dewar, M., & Henstock, T. J. (2020). Broadband acoustic inversion

for gas flux quantification – application to a methane plume at Scanner Pockmark, central North Sea. *Journal of Geophysical Research*, (p. in press). doi:10.1029/2020JC016360.

Løseth, H., Gading, M., & Wensaas, L. (2009). Hydrocarbon leakage interpreted on seismic data. *Marine and Petroleum Geology*, *26*, 1304 – 1319. doi:10.1016/j.marpetgeo.2008.09.008.

MacGregor, L. M., Andreis, D., Tomilinson, J., & Barker, N. (2006). Controlled-source electromagnetic imaging on the Nuggets-1 reservoir. *The Leading Edge*, *25*.

Malinverno, A., Kastner, M., Torres, M. E., & Wortmann, U. G. (2008). Gas hydrate occurrence from pore water chlorinity and downhole logs in a transect across the Cascadia margin (Integrated Ocean Drilling Program Expedition 311). *Journal of Geophysical Research*, *113*.

Marín-Moreno, H., Minshull, T. A., & Edwards, R. A. (2013). A disequilibrium compaction model constrained by seismic data and application to overpressure generation in The Eastern Black Sea Basin. *Basin Research*, *25*, 331–347. doi:10.1111/bre.12001.

McDougall, T. J., & Barker, P. M. (2011). Getting started with TEOS-10 and the Gibbs Seawater (GSW) oceanographic toolbox. *SCOR/IAPSO WG*, *127*, 1–28.

McNeil, J. (1980). Electromagnetic terrain conductivity measurement at low induction numbers. Technical Note TN-6, GEONICS Limited, Ontario, Canada.

Micallef, A., Person, M., Haroon, A., Weymer, B. A., Jegen, M., Schwalenberg, K., Faghih, Z., Duan, S., Cohen, D., Mountjoy, J. J. et al. (2020). 3D characterisation and quantification of an offshore freshened groundwater system in the Canterbury Bight. *Nature communications*, *11*, 1–15.

Morten, J. P., & Bjørke, A. (2020). Imaging and Quantifying CO2 Containment Storage Loss Using 3D CSEM. In *82nd EAGE Annual Conference & Exhibition* (pp. 1–5). European Association of Geoscientists & Engineers volume 2020.

Myer, D., Constable, S., & Key, K. (2011). Broad-band waveforms and robust processing for marine CSEM surveys. *Geophys. J. Int.*, *184*, 689–698.

Naif, S., Key, K., Constable, S., & Evans, R. L. (2015). Water-rich bending faults at the middle america trench. *Geochemistry, Geophysics, Geosystems*, *16*, 2582–2597. doi:10.1002/2015GC005927.

Park, J., Sauvin, G., & Vöge, M. (2017). 2.5D Inversion and Joint Interpretation of CSEM Data at Sleipner CO2 Storage. *Energy Procedia*, *114*, 3989 – 3996. doi:10.1016/j.egypro.2017.03.1531. 13th International Conference on Greenhouse Gas Control Technologies, GHGT-13, 14-18 November 2016, Lausanne, Switzerland.

Peacock, K., & Treitel, S. (1969). Predictive deconvolution - theory and practice. *Geophysics*, *34*, 155–169.

Pearson, C. F., Halleck, P. M., McGuire, P. L., Hermes, R., & Mathews, M. (1983). Natural gas hydrate deposits: A review of in situ properties. *J. Phys. Chem.*, *87*, 4180–4185.

Reinardy, B. T., Hjelstuen, B. O., Sejrup, H. P., Augedal, H., & Jørstad, A. (2017). Late pliocene-pleistocene environments and glacial history of the northern north sea. *Quaternary Science Reviews*, *158*, 107–126.

Riedel, M., Freudenthal, T., Bergenthal, M., Haeckel, M., Wallmann, K., Spangenberg, E., Bialas, J., & Bohrmann, G. (2020). Physical properties and core-log seismic integration from drilling at the Danube deep-sea fan, Black Sea. *Marine and Petroleum Geology*, *114*, 104192. doi:10.1016/j.marpetgeo.2019.104192.

Riedel, M., Long, P., Liu, C., Schultheiss, P., Collett, T., Leg, O., & Party, S. S. (2005). Physical properties of near surface sediments at southern hydrate ridge: results from ODP leg 204. In *Proceedings of the Ocean Drilling Program, Scientific Results*. volume 204.

Robinson, A., Callow, B., Böttner, C., Yilo, N., Provenzano, G., Falcon-Suarez, I. H., Marin-Moreno, H., Lichtschlag, A., Bayrakci, G., Gehrmann, R., Parkes, L., Roche, B., Saleem, U., Schramm, B., Waage, M., Lavayssiére, A., Li, J., Jedari-Eyvazi, F., Sahoo, S., Deusner, C., Kossel, E., Minshull, T. A., Berndt, C., Bull, J. M., Dean, M., James, R., Chapman, M., Best, A. I., Bünz, S., Chen, B., Connelly, D. P., Elger, J., Haeckel, M., Henstock, T. J., Karstens, J., Macdonald, C., Matter, J. M., North, L., & Reinardy, B. (in review). Multiscale characterisation of chimneys/pipes: Fluid escape structures within sedimentary basins. *Int. J. of Greenhouse Gas Control*, .

Sava, D., & Hardage, B. A. (2006). Rock physics characterization of hydrate-

bearing deepwater sediments. *The Leading Edge*, *25*, 616–619. doi:10.1190/1.2202666.

Schwalenberg, K., Gehrmann, R. A. S., Rippe, D., & Bialas, J. (2020). Analysis of marine controlled source electromagnetic data for the assessment of gas hydrates in the Danube deep-sea fan, Black Sea. *Marine and Petroleum Geology*, (p. accepted).

Sinha, M., Patel, P., Unsworth, M., Owen, T., & MacCormack, M. (1990). An active source electromagnetic sounding system for marine use. *Marine Geophysical Researches*, *12*, 59–68.

Stoker, M. S., Balson, P. S., Long, D. M., & Tappin, D. R. (2011). An overview of the lithostratigraphical framework for the Quaternary deposits on the United Kingdom continental shelf. British Geological Survey, Research Report RR/11/03.

Stolt, R. (1978). Migration by Fourier Transform. *Geophysics*, *43*, 23–48.

Weidelt, P. (2007). Guided waves in marine CSEM. *Geophys. J. Int.*, *171*, 153–176.

Weitemeyer, K. A., Constable, S., & Tréhu, A. M. (2011). A marine electromagnetic survey to detect gas hydrate at Hydrate Ridge, Oregon. *Geophys. J. Int.*, (pp. 1–16).

White, J. E. (1975). Computed seismic speeds and attenuation in rocks with partial gas saturation. *Geophysics*, *40*, 224–232. doi:10.1190/1.1440520.

Zhang, X., & Sanderson, D. J. (2002). *Numerical modelling and analysis of fluid flow and deformation of fractured rock masses*. Elsevier.

Appendix A. Phase analysis

The resistivity models shown in the main body of this paper are based on amplitude data only. The information of the phase lag between source and receiver, however, may contain additional information about the resistivity structure in the chimney (see forward models in Fig. A.14 equivalent to the amplitude models in Fig. 4 b and c).

During the processing we apply a time correction to the data depending on the clock synchronisation before and after deployment of the GPS triggered source and the independent quartz clocks in the receiver units. Preliminary analyses have shown that the observed phase data do not match the predicted data, which can be caused by an additional time delay in the hardware or deviation in the navigation that we have not accounted for. Similarly to the static shift in magnetotelluric inversion with MARE2DEM (Key, 2016) we invert for this time delay between the source and receiver timing within each iteration of the model update calculating the residuals of the observed and predicted phase $\delta\varphi = \varphi_\mathrm{o} - \varphi_\mathrm{p}$ and estimating the time delay as an average over all N frequencies with

$$dt = \frac{1}{N}\sum_{i=1}^{N}\frac{\delta\varphi_i}{2\pi f_i}, \tag{A.1}$$

so that the new phase $\varphi'_\mathrm{p} = \varphi_\mathrm{p} + 2\pi f dt$ is updated in every iteration and then used to calculate the data fit. The inversion generally runs slower when including the time delay as an additional parameter and the resistivity model

is not as stable (for example, include artefacts that cannot be explained geologically or do not match between intersecting profiles and seem to depend on the starting model) as without the time delay. Reasons for this are that the update of the model and the time delay estimation are done in two different steps. The data fit is then calculated for the estimated time delay which may bias the weight of phase and amplitude in the update. The result of the time delay is, however, relatively steady in the ms range. To increase the stability of the result and the inversion time, the optimal model of the amplitude only inversions are chosen as the starting model. The inversions were run for profiles P2 to P8 and time delays for the closest receiver range between 13.9 and 24.4 ms and for the furthest receiver between 16.6 and 24.7 ms. The results indicate that the observed phase deviation is indeed caused by a time delay, but it is not clear if it is a receiver or source caused reason. For simplicity first tests were done for one time delay of 16.8 ms added to the transmitter clock for profile P5 for the furthest receiver (Fig. A.15). With the presented technique we can estimate a time delay and fit the phase. Further studies need to be done to estimate the accuracy that is achieved and if the additional analysis adds more information to the resistivity model.

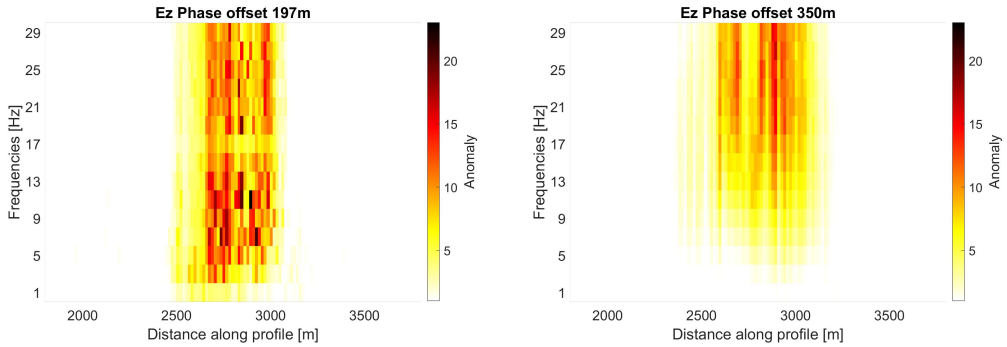

Figure A.14: Data misfit for synthetic phase data for a synthetic model with and without a resistivity increase from 1.2 Ωm to 3.4 Ωm (corresponding to about 35 to 50% free gas depending on the saturation exponent, Fig. 7) at a gas pocket underneath the pockmark for 1 to 29 Hz.

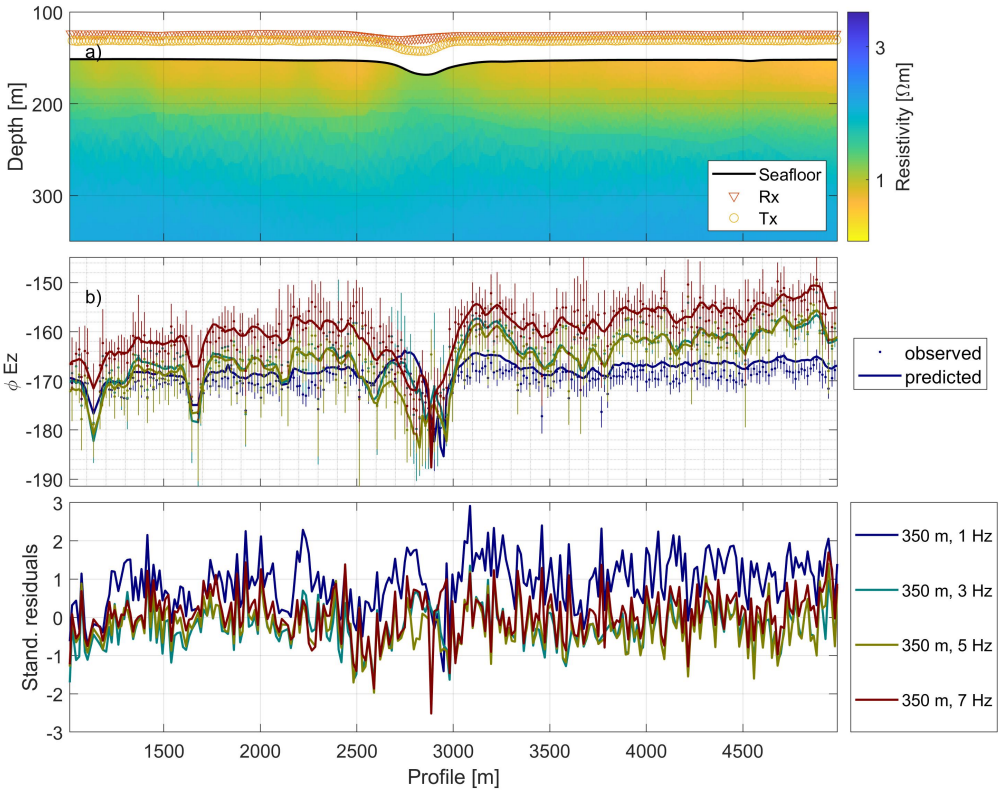

Figure A.15: a) Profile P5 resistivity model for E_z amplitude and phase for the furthest Vulcan without seismic constraints; b) Observed and predicted phase data for 1 to 7 Hz; c) Standardised residuals for phase data (b).